GSA DATA REPOSITORY 2014345

Strong proximal earthquakes revealed by cosmogenic ^{3}He dating of prehistoric rockfalls, Christchurch, New Zealand

B.H. Mackey and M.C. Quigley

1. Cosmogenic sampling and exposure age determination

We used cosmogenic ^{3}He exposure dating to determine the emplacement timing of pre-historic rockfall boulders at Rapaki, Christchurch. Attempts at establishing rockfall depositional ages elsewhere have been made using lichenometry (e.g., Bull, 1996; Bull and Brandon, 1998) or cosmogenic ^{10}Be (e.g., Matmon et al., 2005; Cordes et al., 2013). Cosmogenic isotopes are generated when cosmic rays cause spallation reactions in rock near the Earth's surface, and can be retained in some minerals (e.g., Kurz, 1986; Gosse and Phillips, 2001).

To estimate the emplacement time of paleo-rockfall boulders we took surface samples of rock from the top of 19 of 25 accessible prehistoric basalt boulders with diameters exceeding 1.5 m. The precise location and topographic shielding for each sample was determined by identifying the individual boulders on high-resolution (0.5 m) Lidar-derived topography acquired in Feb 2011 (Canterbury Geotechnical Database, 2013).

We restricted sampling to boulders with top surfaces >0.5 m higher than the surrounding surface to minimize the possibility of post-depositional burial. Samples were obtained from the interfluve between two ephemeral stream channels, rather than the channel beds, where complex burial or post-depositional boulder mobility was more likely. Post-emplacement boulder mobility or intermittent burial can result in underestimation of boulder emplacement age (e.g., Mackey and Lamb, 2013). We only sampled boulders >250 m from the source cliff, as sampling boulders closer to the cliff had an unacceptable level of risk due to ongoing rockfall hazard. Given the overlapping spatial correlation of modern and paleo boulders (Fig 2A) we do not expect any overwhelming bias in the chosen sampling strategy.

We measured ^{3}He in clinopyroxene (augite), a mineral abundant in the Rapaki basalt and quantitatively able to retain ^{3}He (Gosse and Phillips, 2001; Margerison et al., 2005; Deeming et al., 2010). Sample preparation for ^{3}He analysis followed the same procedures outlined in Mackey et al. (2014). We chipped samples off the upper boulder surface, then crushed and sieved the basalt to 500-710 μm grain size. We isolated samples of pure augite using standard magnetic, density, and hand picking techniques. All samples were alternately sonicated in 5% HF:HNO_3 and HCl to remove any surface alteration. Cleaned phenocrysts were ground in a mortar and pestle to <37 um to destroy melt inclusions and release any mantle gas. Approximately 0.3–0.4 g of powdered augite was wrapped in Al foil. Samples were heated under vacuum at 1300 °C and analyzed on a MAP 215-50 mass spectrometer at the California Institute of Technology Noble Gas Laboratory, following Amidon and Farley (2011).

We calculated the exposure age of the boulders and outcrops using the CRONUS ^{3}He online calculator (http://web1.ittc.ku.edu:8888/) (Balco et al., 2008; Goehring et al., 2010) using the 'SA' scaling scheme of Lifton (Lifton et al., 2005) and Sato (Sato and Niita, 2006). Topographic shielding from surrounding topography was calculated from the LiDAR digital elevation model (Codilean, 2006; Li, 2013). We took samples from the underside of some boulders by digging underneath and chipping a sample off base of the boulder, replicating the process used to take top-surface samples.

We use the term 'apparent' exposure age to assume all cosmogenic ^{3}He accumulated while the boulder was position on the hillslope, at a rate determined by the elevation and topographic shielding of the boulder in resting position. This assumption is not valid if there is inherited cosmogenic ^{3}He accrued when the boulder was on the cliff face, as described below.

In older rocks, as is the case with the ~11–12 million year old Lyttelton Volcano (Sewell, 1988; Timm et al., 2009), significant non-cosmogenic ^{3}He and ^{4}He can accumulate in the crystal structure via radioactive decay and neutron capture on ^{6}Li (Lal, 1987). There are several approaches to account for this 'geologic' inheritance (Kurz, 1986; Cerling and Craig, 1994; Blard and Farley, 2008). Here we adopt the use of a shielded sample; one that has been deeply buried and shielded from the effects of cosmic rays at the Earth's surface (e.g., Margerison et al., 2005; Mackey et al., 2014).

Access to recently exposed rock on the cliff face was not possible due to ongoing rockfall risk, so we obtained a formerly shielded sample from the un-exposed side of a large boulder that fell down in the 2011 February earthquake (Fig. DR1). We could identify the detachment face by the distribution of lichen and weathering on the boulder surface. The boulder is sufficiently large (7 × 6 × 3 m), that the samples from the detachment face were buried deeply within the cliff, and shielded from cosmic rays prior to 2011. The shielded samples (Rap25b, Rap25c) have average ^{3}He concentrations of $0.8 \pm 0.1 \times 10^{6}$ at/g (Table DR3). We subtracted this concentration (and propagated associated errors) from each sample to isolate the cosmogenic component of ^{3}He (Table DR3). A sample from the lichen covered face on this boulder (Rap25a) had an apparent exposure age of ~21 ka (2.5×10^{6} at/g ^{3}He), confirming we correctly identified the exposed and shielded faces of the boulder.

We took samples from *in situ* cliff and ridgetop bedrock outcrops to quantify the amount of pre-failure cosmogenic exposure, and to constrain the background erosion rates of basalt in this area. Bedrock exposure ages are presented in Table DR4, and most cluster from 60-70 ka. The oldest bedrock cliff exposure (Rap28, 68±5 ka) equates to a long-term erosion rate of ~7 mm/kyr assuming steady-state erosion. This is calculated using the relationship $E = \Lambda P / N$, where Λ is the e-folding length of cosmic ray flux at the Earth's surface (~160 g/cm^2, about 0.5 m in basalt), P the nuclide production rate (at/g/yr), and N the measured concentration of atoms at the rock surface (Lal, 1991). We calculated the exposure age of boulders under two scenarios; first assuming no erosion, and second with the 7 mm/kyr erosion rate as an upper constraint (Table DR4). While this has a major effect on the exposure ages of the older boulders, the determined influence of erosion on the exposure ages of the Holocene boulders is negligible (<5%).

A further complication is post-depositional boulder mobility, which can create complicated cosmogenic concentration profiles. In this instance, the presence of a thick colluvial wedge that has accumulated upslope of the boulders (Fig 2A), with only a thin (<10 cm) soil-filled, downward tapering wedge against the boulder edge, together with the lack of prehistoric boulder remobilization in the Christchurch earthquakes indicates minimal post-depositional boulder remobilization.

2. Cosmogenic inheritance

A consideration when using cosmogenic nuclides to date boulder emplacement via rockfall is a prior history of cosmogenic exposure, referred to as inheritance. To illustrate this, a survey of large (>1 m diameter) boulders which fell at Rapaki during the 2011 earthquakes revealed that 45% (26 of 57 surveyed) landed with a previously exposed side facing upright, as indicated by the orientation of lichen cover and surface weathering (e.g., Fig 2D).

The cliff face is sub-vertical, but pre-failure exposed faces of boulders could have been vertical to sub-horizontal, depending whether they fell from cliff faces or ledges (Fig. DR2A). The penetration of cosmic ray flux into a vertical surface has an e-folding length of approximately 0.2 m, less than half the equivalent length-scale for rocks on a horizontal surface (Dunne et al., 1999; Dunne and Elmore, 2003), such that a rock surface set 0.5 m into a vertical cliff is ~95% shielded from cosmic flux (Figure DR2B).

The large (>1.5 m diameter) dimensions of the sampled rockfall boulders and the sub-vertical orientation of the source cliff dictates that some presently exposed boulder top surfaces will have been partially or fully self-shielded from cosmic rays while exposed on the cliff prior to detachment and deposition (Figure DR2C). Other rockfall boulder surfaces may have formerly been completely exposed to cosmic rays as horizontal (tops of rock surfaces) or vertical (exposed vertical cliff face) surfaces, or partially self-shielded within the rock mass. As a consequence, a population of boulders mobilized in an earthquake will be deposited with no (or minimal) inherited ^{3}He on the top surface and the cosmogenic surface exposure age will be equivalent to the boulder emplacement age. Another population of boulders will have varying components of pre-detachment, inherited cosmogenic ^{3}He in addition to that acquired following deposition. The pre-detachment orientation of individual paleo-rockfall boulders cannot be determined by field observations due to extensive lichen cover, extensive cliff collapse in the Christchurch earthquakes, and the possibility of post-detachment boulder disintegration while mobile.

We sampled the underside of the younger (6-8 ka) boulders, and all four undersides had ^{3}He concentrations significantly higher than the shielded sample. We interpret this to indicate the top surface of these boulders was originally a detachment face within the cliff, shielded from cosmic rays, prior to a triggering event that emplaced the boulders ‘fresh’ side up at ~ 7 ka. Conversely, boulder Rap04 has an apparent surface exposure age of 50 ka and has no cosmogenic ^{3}He on the underside (Rap04b), suggesting it was emplaced with a previously-exposed side up (detachment surface facing down) at an unknown time.

3. Modeling paleo-rockfall scenarios

We sought to replicate the observed behavior of rockfalls and expected cosmogenic age for a range of earthquake scenarios. Based on our observations on the resting orientation of modern rockfall boulders, and realistic exposure histories for boulders on a cliff face, we modeled rockfall boulder age populations for the three simple earthquake scenarios described in the text.

As discussed in the text, cubic-shaped boulders have a 0.17 probability of landing exposed side down, and a 0.17 probability of landing exposed side up. Boulders that landed on their side with respect to the original exposed surface (0.66 probability) have a partially shielded top surface. Partial shielding was calculated by modifying the external (cliff face) age of the boulder with a function to simulate the e-folding decay of cosmogenic production into rock.

We assigned each boulder face a random depth from 0 to 2 m to replicate the range of rockfall boulder sizes (up to ~4 m). We then modified the surface age with an exponential depth function to replicate the decay of cosmic ray flux intensity into rock. In this way we replicate boulder surfaces that may have been partially shielded in the cliff. For example, a 10 ka boulder with a surface concentration (N_0), assigned a random depth (z) of 0.5 m would be modified by $N(z) = N_0 e^{-z\rho/\Lambda}$, (where ρ is density (2.6 g/cm^3) and Λ, is attenuation length, (~160 g/cm^2)), to have an apparent exposure age of 4.6 ka when emplaced deposited. All rockfall scenarios had a final boulder population of 100. Each simulation was replicated 1000 times, and we averaged the relative probability distributions across all the simulations to generate the synthetic curves in Fig 3B.

4. Regional fault sources, predicted Peak Ground Velocities, and rockfall-triggering potential

Recent compilations of mapped active faults in New Zealand (Stirling et al., 2012; Litchfield et al., 2013) included in latest version of the New Zealand Seismic Hazard Model (NZSHM) (Stirling et al., 2012) were used to provide seismic source information on earthquake shaking and possible rockfall triggering potential at the Rapaki study site. We compiled published estimates of maximum moment magnitude (M_w^{max}) and earthquake recurrence intervals (RI) from NZSHM faults in the south-central New Zealand (Stirling et al., 2012; Litchfield et al., 2013). M_w^{max} for offshore faults in Pegasus Bay (Barnes et al., 2011) were derived using measured lengths and a New Zealand-specific magnitude regression equation (Stirling et al., 2008) that was used in the NZSHM (Stirling et al., 2012):

$$M_W = 4.18 + 2/3 \log W + 4/3 \log L \qquad (1)$$

where L is fault length in kilometers and W is fault width in kilometers. We assumed vertical faults and used W = 12 km for Pegasus Bay M_w^{max} calculations. Tentative RI estimates for Pegasus Bay faults are >10–20 kyr (Barnes et al., 2011) (Figure 1). We measured the minimum distance of all active fault surface rupture traces to the study site (R_{Rup}). Known active faults are color-coded by RI increments in Figure DR3.

Importantly, RIs are poorly defined for many faults, and the absence or discordance between paleo-earthquakes on specific sources and the Rapaki paleo-rockfall events can only be used in a few instances (e.g., Alpine Fault, Porter's Pass Fault) to exclude a fault as a culpable source for paleo-rockfalls. For instance, poorly resolved chronologies from the nearby Springbank and Ashley faults (M_w 7-7.2, recurrence intervals of ca. 5-7 kyr) (Stirling et al., 2012) with no robust constraints on timing of the most recent earthquakes on these faults prohibits their exclusion as possible rockfall-triggering sources on temporal grounds alone.

We input M_w^{max} and R_{Rup} into New Zealand-specific ground motion prediction equations (GMPEs) established by Bradley (2013) (based on global models of Chiou and Youngs (2008)) to predict peak ground velocities (PGV) at the base of the study site for earthquakes of M_w^{max} from all known sources. The average shear wave velocity in the top 30 meters of crust (Vs30) was assumed to be 800 m/s. Variations in rupture directivity, which are known to influence strong ground motion characteristics (Somerville et al., 1997) and which were particularly prevalent in the Darfield earthquake (Bradley, 2012) are not explicitly considered in the developed GMPE and thus were not considered in this analysis. GMPE-based PGVs were also derived for the M_w 7.1 September 2010 (Darfield), M_w 6.2 February 2011 (Christchurch I), M_w 6.0 June 2011 (Christchurch II-b), and M_w 5.9 December 2011

(Christchurch III-b) earthquakes. The GMPE-based PGV's are lower than instrumental values because strong ground motions recorded by the latter are amplified due to site effects and topography. For instance, LPCC is not actually a 'true' rock site in that it sits on several meters of rock fill and this causes some amplification relative to that of the surrounding rock. D13C and D15C are at high elevations along broad ridges where seismic waves will be focused and amplified relative to waves at the base of the Port Hills in analogous material. The methodology for horizontal PGV calculations (PGV_H^{max}) for CES events based on linear interpolation of instrumental data is discussed in the text.

Rockfall at the study site that resulted in boulders being deposited on the portion of slope studied herein occurred only during the Christchurch I and II-b earthquakes. Rare and isolated rockfall was reported by some local residents to M. Quigley to have occurred in proximal areas during the Darfield and Christchurch III-b earthquakes, but this did not result in any detachment of large boulders from the source cliff or any boulder deposition on the slope encompassed by this study. A rockfall initiation 'threshold' GMPE-derived PGV value of ~13±2 cm /s is used, with a minimum value equivalent to the GMPE predicted PGV for the Darfield earthquake (11 cm/s) because minor localized rockfall was observed nearby in this event, and maximum value (~15 cm/s) below GMPE predicted PGV for the Christchurch I and II-b events (17 cm/s). The PGV threshold value represents a minimum input value at the base of the hillslope only, rather than the absolute PGV at which rocks are able to be detached from the source cliff. GMPE-predicted PGV values from all identified seismic sources in the NZSHM are then compared to this threshold value.

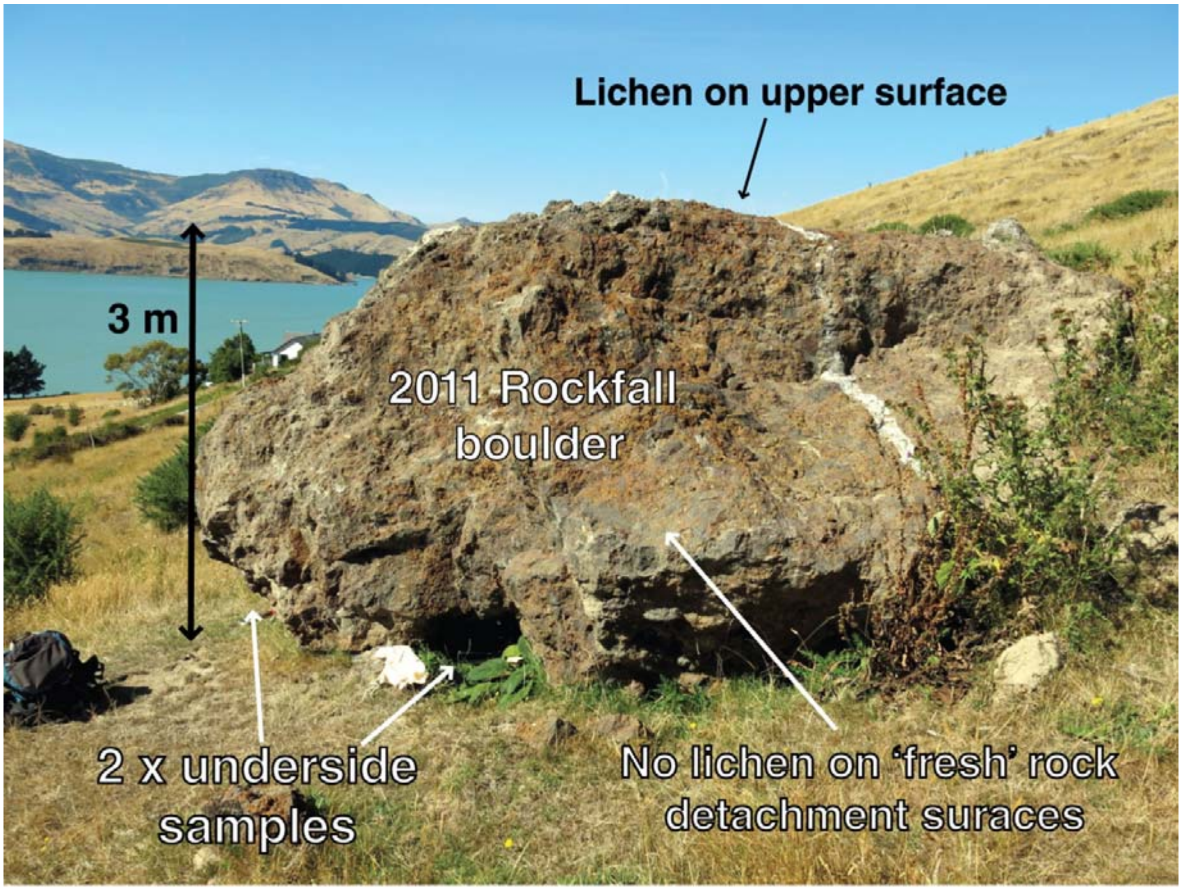

Figure DR1: Large boulder which fell down in the February 22 2011 earthquake, and travelled ~500 m from the cliff face. This boulder was used to establish background (shielded) concentrations of ^{3}He. Two samples taken from the base of the boulder were formerly shielded from cosmic rays within the cliff mass, and have ^{3}He concentrations of $0.8 \pm 0.1 \times 10^{6}$ at/g.

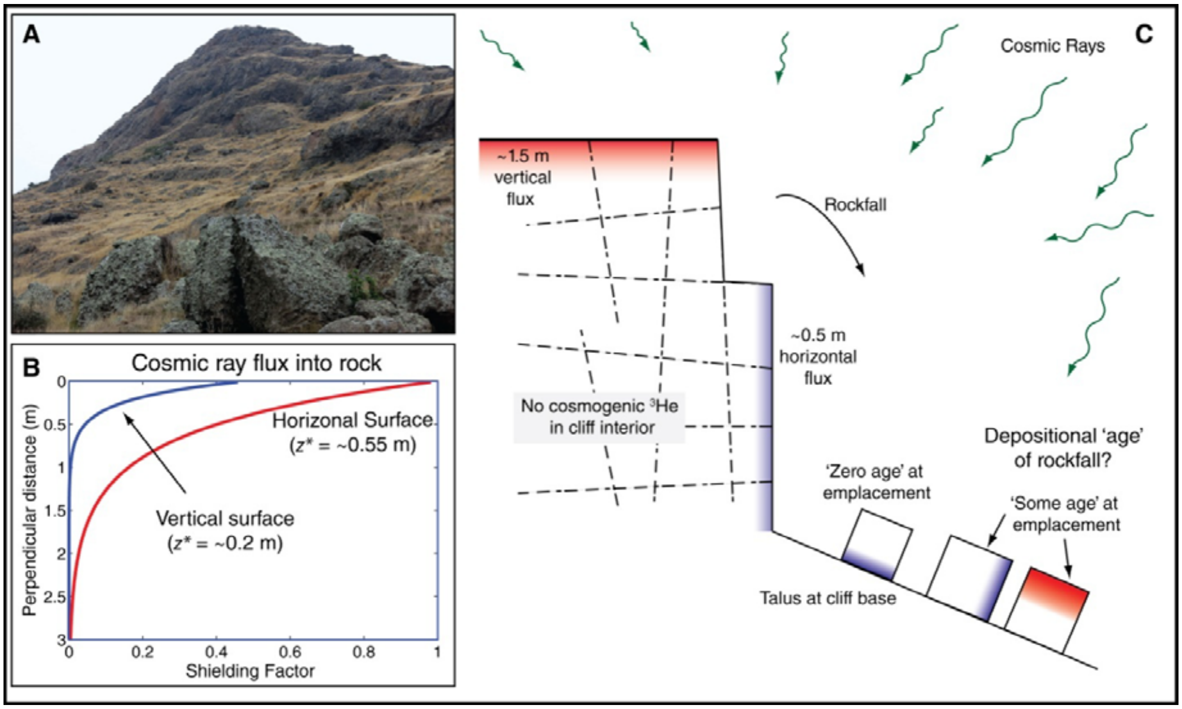

Figure DR2: (A) View looking up at the cliff, the source of the rockfall boulders. (B) Depth profiles of cosmic ray flux into vertical and horizontal bedrock, relative to a flat horizontal surface. The e-folding length of flux decay into a vertical cliff (0.2 m) is less than half that for an equivalent horizontal surface (after Dunne et al., 1999). (C) Cartoon cross section of cliff and depositional slope showing cosmogenic exposure and inheritance on ridge and cliff face. Boulders fall off the cliff and land with three possible orientations, relative to prior exposure they received on the cliff face (blue) or ridge/ledge (red).

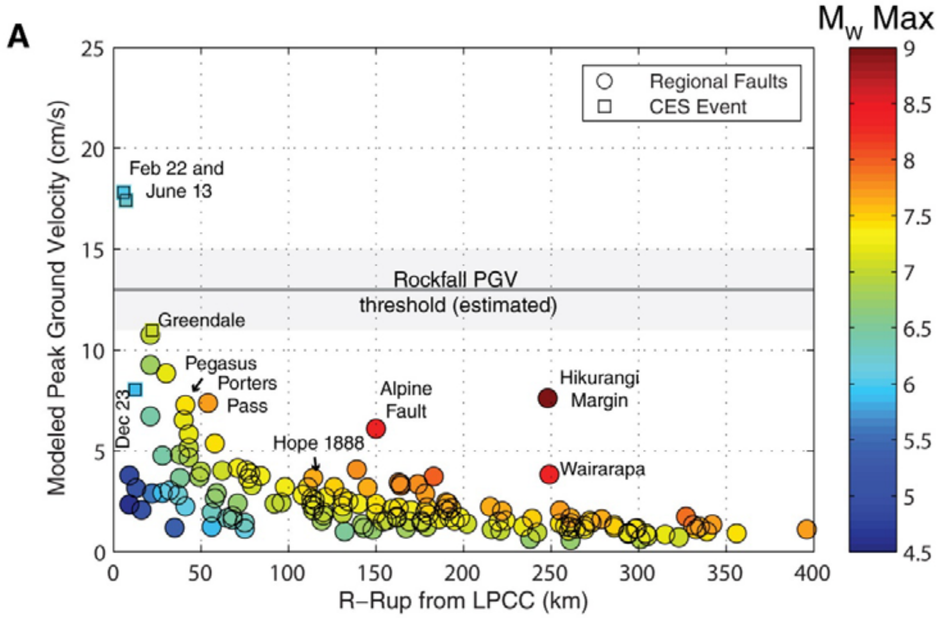

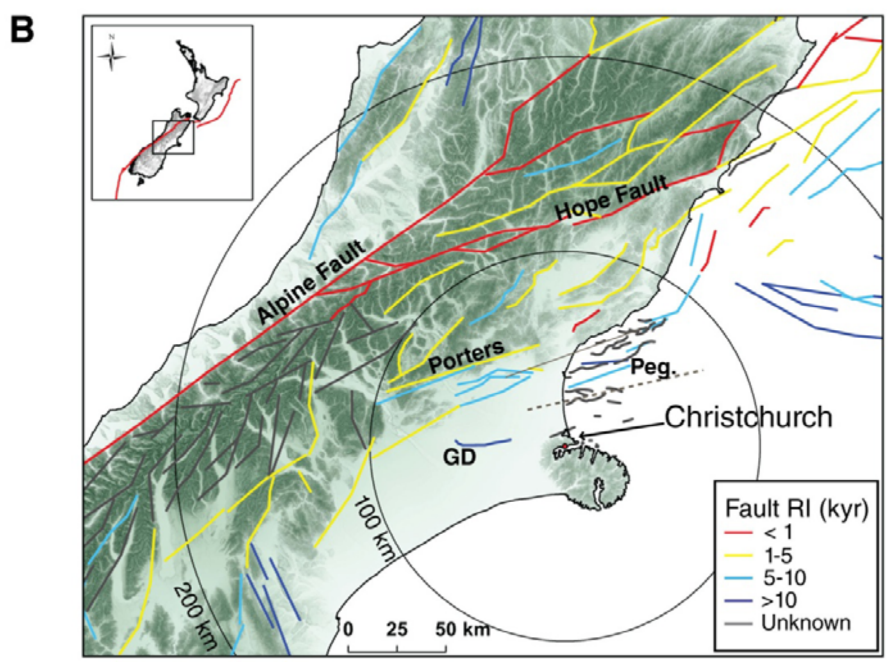

Figure DR3: (A) GMPE-modeled peak ground velocities at Lyttelton Port seismic station (LPCC). Modeled PGV based on max M_W and closest distance (R_{Rup}) to known regional fault sources. Modeled PGV for regional faults is below modeled PGV threshold for rockfall initiation (~13 ± 2 cm/s) derived from observations in the CES. (B) Identified South Island Faults modeled in (A). Faults are colored by recurrence interval. Circles are 100 and 200 km radius distance from LPCC. Major faults labeled (Greendale (GD), Pegasus (Peg.). Inset shows location in NZ with the plate boundary in red.

Table DR1. Location and site information of strong ground motion seismometers for which data was used in this study. All station information and strong ground motion data available at *http://info.geonet.org.nz/display/appdata/Strong-Motion+Data* (last accessed 9 July 2014).

Station code	Location	Elevation (m asl)	Geology	Distance to source cliff (km)
D13C	Lat: -43.6083 Lon: 172.6447	467	Rock	2.3
LPCC	Lat:-43.6078 Lon: 172.7247	0	Weathered rock	4.3
D15C	Lat: -43.5864 Lon: 172.7256	339	Rock	4.7
CRLZ	Lat: -43.5764 Lon: 172.6231	55	Cave (Rock)	4.9
STUDY SITE	Lat:-43.6022 Lon: 172.6718	270	Rock	0

Table DR2. Location and site information of strong ground motion seismometers for which data was used in this study

Earthquake (Date)	Stn or study site	Epicentral distance (km)	PGV_H^{max} cm/s	Mw	Rockfall ?
Darfield	CRLZ	37	16.1	7.2	minor
(04/09/2010)	LPCC	46	18.6		
(Greendale Fault)	**STUDY SITE**	**41**	**17.2**		
Christchurch I	LPCC	5	47.6	6.2	major
(22/02/2011)	**STUDY SITE**	**2.5**	**47.6**		
April	D13C	9	3.5	5	no
(16/04/2011)	D15C	3	27.0		
	STUDY SITE	**7**	**11.4**		
Christchurch II-a	CRLZ*	10	6.9	5.3	moderate
(13/06/2011)	LPCC*	4	6.9		
	D13C	9	10.2		
	D15C	2	12.3		
	STUDY SITE	**7**	**10.8**		
Christchurch II-b	CRLZ	9	19.7	6	major
(13/06/2011)	LPCC	4	43.0		
	D13C	9	24.8		
	D15C	2	53.4		
	STUDY SITE	**6.5**	**33.1**		
Christchurch III-a	CRLZ	18	6.5	5.8	no
(23/12/2011)	LPCC	15	10.8		
	D13C	19	5.9		
	D15C	13	10.6		
	STUDY SITE	**17**	**7.8**		
Christchurch III-b	CRLZ	12	8.9	5.9	minor
(23/12/2011)	LPCC*	10	27.4		
	D13C	13	8.0		
	D15C	7	21.5		
	STUDY SITE	**10.8**	**12.5**		

* not used in STUDY SITE calculation

Table DR3.

Helium data from fusion of augite samples. Subscript 'melt' is helium released by heating powdered augite under vacuum. R/R_A is the measured $^3He/^4He$ ratio divided by the atmospheric $^3He/^4He$ isotope ratio of 1.4×10^{-6}. Symbol 'at' denotes atoms.

Sample	Mass (g)	$^3He_{melt}$ (10^6 at/g)	± 1σ	$^4He_{melt}$ (10^{12} at/g)	± 1σ	R/R_A Melt
Rap01	0.4088	1.73	0.10	2.48	0.12	0.50
Rap01b	0.3536	1.47	0.09	2.76	0.14	0.38
Rap02	0.4727	3.97	0.24	4.84	0.24	0.59
Rap02b	0.3194	4.34	0.26	2.29	0.11	1.35
Rap03	0.3488	1.77	0.11	2.89	0.14	0.44
Rap03a	0.3721	4.39	0.26	2.27	0.11	1.38
Rap04	0.4214	7.04	0.42	2.65	0.13	1.90
Rap04b	0.3234	0.74	0.04	2.42	0.12	0.22
Rap05	0.3525	2.28	0.14	3.72	0.19	0.44
Rap06	0.3295	1.83	0.11	3.64	0.18	0.36
Rap06a	0.3631	1.87	0.11	2.00	0.10	0.67
Rap07	0.372	4.21	0.25	3.27	0.16	0.92
Rap08	0.3379	2.69	0.16	3.96	0.20	0.49
Rap09	0.3915	2.17	0.13	2.37	0.12	0.65
Rap10	0.3699	3.35	0.20	2.69	0.13	0.89
Rap11	0.389	2.76	0.17	3.61	0.18	0.55
Rap12	0.3341	2.60	0.16	5.15	0.26	0.36
Rap13	0.383	2.10	0.13	3.18	0.16	0.47
Rap15	0.3703	2.37	0.14	2.69	0.13	0.63
Rap16	0.3655	1.59	0.10	3.48	0.17	0.33
Rap17	0.3195	10.29	0.62	4.05	0.20	1.82
Rap18	0.3968	2.51	0.15	2.63	0.13	0.68
Rap19	0.3597	1.58	0.10	2.24	0.11	0.51
Rap27	0.3694	2.38	0.14	2.96	0.15	0.57
Rap21a	0.0642	6.43	0.39	2.19	0.11	2.10
Rap23	0.3482	5.41	0.32	3.17	0.16	1.22
Rap24	0.3669	10.36	0.62	1.93	0.10	3.83
Rap28	0.3901	10.00	0.60	1.98	0.10	3.61
Rap29	0.3803	7.21	0.43	2.09	0.10	2.46
Rap25a	0.3637	3.28	0.20	2.47	0.12	0.95
Rap25b	0.3418	0.86	0.05	3.44	0.17	0.18
Rap25c	0.3824	0.69	0.04	2.55	0.13	0.19

Table DR4. Cosmogenic ^{3}He exposure ages. [^{3}He]$_c$ is the cosmogenic component of ^{3}He, after subtracting the shielded sample concentration (Rap25b, Rap25c, Table DR3). ^{3}He production rates and exposure ages were calculated using the CRONUS ^{3}He calculator using the Lifton/Sato "SA" scaling scheme. Two age scenarios are given, 1 assuming no erosion, and the second assuming a background erosion rate of 7 mm/kyr. Basalt had a bulk density of 2.6 ± 0.1 g/cm^3. Error represents ± 1σ. Production and exposure age is calculated for the resting position of the boulder, and assuming all [^{3}He]$_c$ accumulated after deposition. Bedrock exposure ages were calculated from the orientation of the sampled face. Rap 21A was taken from a slab that detached from a sub-vertical cliff in 2011 and slid down the hillslope (visible in Fig. 2D). The pre-failure location of the rock slab could be determined. All samples include a self-shielding correction of 0.976.

Sample	Comment	long	lat	Elevation (m)	Topo shield	[^{3}He]$_c$	±σ	^{3}He prodn (at/g/yr)	Apparent exposure age (ka)	±σ	Age with erosion (ka)	±σ
Paleo-rockfall boulders												
Rap01	Boulder top	172.6778	-43.6038	67	0.97	0.96	0.22	115	8.1	2.1	8.5	2.2
Rap01b	Underside	172.6778	-43.6038	67	0.97	0.69	0.21	115	5.9	1.6	6.1	1.7
Rap02	Boulder top	172.6771	-43.6038	81	0.97	3.19	0.36	116	26.9	2.9	32.0	4.2
Rap02b	Underside	172.6771	-43.6038	81	0.97	3.56	0.38	116	30.0	3.1	36.5	4.8
Rap03	Boulder top	172.6765	-43.6035	96	0.98	0.99	0.22	119	8.1	1.9	8.6	2.2
Rap03a	Underside	172.6766	-43.6035	95	0.92	3.61	0.38	112	31.7	3.3	39.0	5.2
Rap04	Boulder top	172.6760	-43.6030	110	0.98	6.26	0.54	120	50.3	4.5	75.1	12.4
Rap04b	Underside	172.6760	-43.6030	110	0.98	-0.04	0.16	120	0.0	0.0	0.0	0.0
Rap05	Boulder top	172.6757	-43.6031	116	0.97	1.50	0.26	120	12.5	2.2	13.4	2.5
Rap06	Boulder top	172.6759	-43.6028	116	0.98	1.05	0.23	121	8.5	2.0	9.0	2.2
Rap06a	Underside	172.6759	-43.6028	115	0.92	1.09	0.23	113	9.5	2.1	10.0	2.3
Rap07	Boulder top	172.6758	-43.6027	119	0.98	3.43	0.37	121	27.8	2.9	33.3	4.3
Rap08	Boulder top	172.6758	-43.6023	124	0.98	1.91	0.28	122	15.7	2.3	17.2	2.8
Rap09	Boulder top	172.6763	-43.6042	97	0.97	1.40	0.25	118	11.8	2.1	12.7	2.6
Rap10	Boulder top	172.6762	-43.6039	102	0.98	2.57	0.32	120	21.3	2.5	24.3	3.4
Rap11	Boulder top	172.6767	-43.6045	83	0.98	1.98	0.28	118	16.8	2.4	18.6	2.9

Rap12	Boulder top	172.6762	-43.6039	102	0.98	1.82	0.27	120	15.2	2.3	16.7	2.9
Rap13	Boulder top	172.6762	-43.6039	101	0.98	1.33	0.24	120	11.0	2.0	11.8	2.5
Rap15	Boulder top	172.6754	-43.6036	129	0.98	1.59	0.26	122	13.0	2.3	14.0	2.5
Rap16	Boulder top	172.6753	-43.6040	130	0.98	0.81	0.21	122	6.5	1.6	6.7	1.8
Rap17	Boulder top	172.6740	-43.6037	179	0.97	9.51	0.74	127	72.5	5.7	153.0	52.3
Rap18	Boulder top	172.6747	-43.6038	153	0.97	1.73	0.27	124	14.0	2.1	15.2	2.5
Rap19	Boulder top	172.6749	-43.6040	143	0.97	0.81	0.21	124	6.4	1.6	6.6	1.7
Rap27	Boulder top	172.6758	-43.6034	116	0.98	1.60	0.26	121	13.2	2.2	14.3	2.5
Bedrock surfaces												
Rap21a	2011 cliff	172.6734	-43.5997	220	0.60	5.66	0.50	82	66.9	7.1	125.8	33.7
Rap23	Ridge exposure	172.6697	-43.6031	396	1.00	4.63	0.44	160	28.4	2.6	34.1	4.0
Rap24	Ridge exposure	172.6693	-43.6029	393	1.00	9.58	0.74	160	58.0	4.5	95.3	17.1
Rap28	Cliff exposure	172.6735	-43.6018	204	0.98	9.23	0.72	131	68.2	5.4	131.3	35.4
Rap29	Cliff exposure	172.6735	-43.6018	201	0.75	6.43	0.55	101	61.8	5.2	106.8	22.9
Shielded sample boulder												
Rap25a	2011 cliff	172.6769	-43.6043	82	0.98	2.51	0.32	118	21.1	2.5	24.0	3.4

Data Repository References

Amidon, W.H., and Farley, K.A., 2011, Cosmogenic He-3 production rates in apatite, zircon and pyroxene inferred from Bonneville flood erosional surfaces: Quaternary Geochronology, v. 6, no. 1, p. 10-21, doi:10.1016/j.quageo.2010.03.005

Balco, G., Stone, J.O., Lifton, N.A., and Dunai, T.J., 2008, A complete and easily accessible means of calculating surface exposure ages or erosion rates from Be-10 and Al-26 measurements: Quaternary Geochronology, v. 3, no. 3, p. 174-195, doi:10.1016/j.quageo.2007.12.001

Barnes, P.M., Castellazzi, C., Gorman, A., and Wilcox, S., 2011, Submarine Faulting Beneath Pegasus Bay, Offshore Christchurch: Wellington, National Institute of Water and Atmospheric Research Ltd (NIWA), Report WLG2011-28, p. 46

Blard, P.H., and Farley, K.A., 2008, The influence of radiogenic He-4 on cosmogenic He-3 determinations in volcanic olivine and pyroxene: Earth and Planetary Science Letters, v. 276, no. 1-2, p. 20-29, doi:10.1016/j.epsl.2008.09.003

Bradley, B.A., 2012, Ground motions observed in the Darfield and Christchurch earthquakes and the importance of local site response effects: New Zealand Journal of Geology and Geophysics, v. 55, no. 3, p. 279-286, doi:10.1080/00288306.2012.674049

Bradley, B.A., 2013, A New Zealand-specific pseudospectral acceleration ground-motion prediction equation for active shallow crustal earthquakes based on foreign models: Bulletin of the Seismological Society of America, v. 103, no. 3, p. 1801-1822, doi:10.1785/0120120021

Bull, W.B., 1996, Dating San Andreas fault earthquakes with lichenometry: Geology, v. 24, no. 2, p. 111-114, doi:10.1130/0091-7613(1996)024<0111:dsafew>2.3.co;2

Bull, W.B., and Brandon, M.T., 1998, Lichen dating of earthquake-generated regional rockfall events, Southern Alps, New Zealand: Geological Society of America Bulletin, v. 110, no. 1, p. 60-84, doi:10.1130/0016-7606(1998)110<0060:ldoegr>2.3.co;2

Canterbury Geotechnical Database (2012) "LiDAR and Digital Elevation Models", Map Layer CGD0500 23 July 2012, retrieved 10 June 2013 from https://canterburygeotechnicaldatabase.projectorbit.com

Cerling, T.E., and Craig, H., 1994, Geomorphology and in-situ cosmogenic isotopes: Annual Review of Earth and Planetary Sciences, v. 22, p. 273-317

Chiou, B.-J., and Youngs, R.R., 2008, An NGA model for the average horizontal component of peak ground motion and response spectra: Earthquake Spectra, v. 24, no. 1, p. 173-215, doi:10.1193/1.2894832

Codilean, A.T., 2006, Calculation of the cosmogenic nuclide production topographic shielding scaling factor for large areas using DEMs: Earth Surface Processes and Landforms, v. 31, no. 6, p. 785-794, doi:10.1002/esp.1336

Cordes, S.E., Stock, G.M., Schwab, B.E., and Glazner, A.F., 2013, Supporting evidence for a 9.6 ± 1 ka rock fall originating from Glacier Point in Yosemite Valley, California: Environmental & Engineering Geoscience, v. 19, no. 4, p. 345-361, doi:10.2113/gseegeosci.19.4.345

Deeming, K.R., McGuire, B., and Harrop, P., 2010, Climate forcing of volcano lateral collapse: evidence from Mount Etna, Sicily: Philosophical Transactions: Mathematical, Physical and Engineering Sciences, v. 368, no. 1919, p. 2559-2577, doi:10.2307/25753428

Dunne, J., Elmore, D., and Muzikar, P., 1999, Scaling factors for the rates of production of cosmogenic nuclides for geometric shielding and attenuation at depth on sloped surfaces: Geomorphology, v. 27, no. 1-2, p. 3-11

Dunne, J.A., and Elmore, D., 2003, Monte Carlo simulations of low-energy cosmogenic neutron fluxes near the bottom of cliff faces: Earth and Planetary Science Letters, v. 206, no. 1-2, p. 43-49

Goehring, B.M., Kurz, M.D., Balco, G., Schaefer, J.M., Licciardi, J., and Lifton, N., 2010, A reevaluation of *in situ* cosmogenic ^{3}He production rates: Quaternary Geochronology, v. 5, no. 4, p. 410-418, doi:10.1016/j.quageo.2010.03.001

Gosse, J.C., and Phillips, F.M., 2001, Terrestrial in situ cosmogenic nuclides: theory and application: Quaternary Science Reviews, v. 20, no. 14, p. 1475-1560

Kurz, M.D., 1986, In situ production of terrestrial cosmogenic Helium and some applications to geochronology: Geochimica et Cosmochimica Acta, v. 50, no. 12, p. 2855-2862

Lal, D., 1987, Production of He-3 in terrestrial rocks: Chemical Geology, v. 66, no. 1-2, p. 89-98

Lal, D., 1991, Cosmic-ray labeling of erosion surfaces - Insitu nuclide production-rates and erosion models: Earth and Planetary Science Letters, v. 104, no. 2-4, p. 424-439

Lamb, M.P., Mackey, B.H., and Farley, K.A., 2014, Amphitheater-headed canyons formed by megaflooding at Malad Gorge, Idaho: Proceedings of the National Academy of Sciences, v. 111, no. 1, p. 57-62, doi:10.1073/pnas.1312251111

Li, Y.-k., 2013, Determining topographic shielding from digital elevation models for cosmogenic nuclide analysis: a GIS approach and field validation: Journal of Mountain Science, v. 10, no. 3, p. 355-362, doi:10.1007/s11629-013-2564-1

Lifton, N.A., Bieber, J.W., Clem, J.M., Duldig, M.L., Evenson, P., Humble, J.E., and Pyle, R., 2005, Addressing solar modulation and long-term uncertainties in scaling secondary cosmic rays for in situ cosmogenic nuclide applications: Earth and Planetary Science Letters, v. 239, no. 1–2, p. 140-161, doi:http://dx.doi.org/10.1016/j.epsl.2005.07.001

Litchfield, N.J., Van Dissen, R., Sutherland, R., Barnes, P.M., Cox, S.C., Norris, R., Beavan, R.J., Langridge, R., Villamor, P., Berryman, K., Stirling, M., Nicol, A., Nodder, S., Lamarche, G., Barrell, D.J.A., Pettinga, J.R., Little, T., Pondard, N., Mountjoy, J.J., and Clark, K., 2013, A model of active faulting in New Zealand: New Zealand Journal of Geology and Geophysics, v. 57, no. 1, p. 32-56, doi:10.1080/00288306.2013.854256

Mackey, B.H., and Lamb, M.P., 2013, Deciphering boulder mobility and erosion from cosmogenic nuclide exposure dating: Journal of Geophysical Research: Earth Surface, v. 118, no. 1, p. 184-197, doi:10.1002/jgrf.20035

Mackey, B.H., Scheingross, J.S., Lamb, M.P., and Farley, K.A., 2014, Knickpoint formation, rapid propagation, and landscape response following coastal cliff retreat at the last interglacial sea-level highstand: Kaua'i, Hawai'i: Geological Society of America Bulletin, doi:10.1130/b30930.1

Margerison, H.R., Phillips, W.M., Stuart, F.M., and Sugden, D.E., 2005, Cosmogenic ^{3}He concentrations in ancient flood deposits from the Coombs Hills, northern Dry Valleys, East Antarctica: interpreting exposure ages and erosion rates: Earth and Planetary Science Letters, v. 230, no. 1–2, p. 163-175, doi:10.1016/j.epsl.2004.11.007

Matmon, A., Shaked, Y., Porat, N., Enzel, Y., Finkel, R., Lifton, N., Boaretto, E., and Agnon, A., 2005, Landscape development in an hyperarid sandstone environment along the margins of the Dead Sea fault: Implications from dated rock falls: Earth and Planetary Science Letters, v. 240, no. 3–4, p. 803-817, doi:http://dx.doi.org/10.1016/j.epsl.2005.06.059

Sato, T., and Niita, K., 2006, Analytical functions to predict cosmic-ray neutron spectra in the atmosphere: Radiation Research, v. 166, no. 3, p. 544-555, doi:10.1667/rr0610.1

Sewell, R.J., 1988, Late Miocene volcanic stratigraphy of central Banks Peninsula, Canterbury, New Zealand: New Zealand Journal of Geology and Geophysics, v. 31, no. 1, p. 41-64, doi:10.1080/00288306.1988.10417809

Somerville, P.G., Smith, N.F., Graves, R.W., and Abrahamson, N.A., 1997, Modification of empirical strong ground motion attenuation relations to include the amplitude and duration effects of rupture directivity: Seismological Research Letters, v. 68, no. 1, p. 199-222, doi:10.1785/gssrl.68.1.199

Stirling, M., Gerstenberger, M., Litchfield, N., McVerry, G., Smith, W., Pettinga, J., and Barnes, P., 2008, Seismic hazard of the Canterbury region, New Zealand: New earthquake source model and methodology: Bulletin of the New Zealand Society for Earthquake Engineering, v. 41, no. 2, p. 51-67

Stirling, M., McVerry, G., Gerstenberger, M., Litchfield, N., Van Dissen, R., Berryman, K., Barnes, P., Wallace, L., Villamor, P., Langridge, R., Lamarche, G., Nodder, S., Reyners, M., Bradley, B., Rhoades, D., Smith, W., Nicol, A., Pettinga, J., Clark, K., and Jacobs, K., 2012, National seismic hazard model for New Zealand: 2010 Update: Bulletin of the Seismological Society of America, v. 102, no. 4, p. 1514-1542, doi:10.1785/0120110170

Timm, C., Hoernle, K., Van Den Bogaard, P., Bindeman, I., and Weaver, S., 2009, Geochemical evolution of intraplate volcanism at Banks Peninsula, New Zealand: Interaction between asthenospheric and lithospheric melts: Journal of Petrology, v. 50, no. 6, p. 989-1023, doi:10.1093/petrology/egp029